Electronic Supplementary Material (ESI) for Inorganic Chemistry Frontiers.

Cyanide-bridged coordination polymers constructed from lanthanide ions and octacyanometallate building-blocks

Yuan Gao,[a] Marta Viciano-Chumillas,[b] Ana Maria Toader,[c] Simon J. Teat,[d] Marilena Ferbinteanu,[e]* Stefania Tanase[a]*

[a]Van 't Hoff Institute for Molecular Sciences, University of Amsterdam, Science Park 904, 1098XH Amsterdam, The Netherlands. E-mail: s.grecea@uva.nl

[b]Instituto de Ciencia Molecular (ICMol), Universidad de Valencia, c/ Catedrático José Beltrán, 2, 46980 Paterna, Spain.

[c]Institute of Physical Chemistry, Splaiul Independentei 202, Bucharest 060021, Romania.

[d]Advanced Light Source, Lawrence Berkeley National Laboratory, Berkeley, USA.

[e]Faculty of Chemistry, Inorganic Chemistry Department, University of Bucharest, Dumbrava Rosie 23, Bucharest 020462, Romania. E-mail: marilena.cimpoesu@g.unibuc.ro

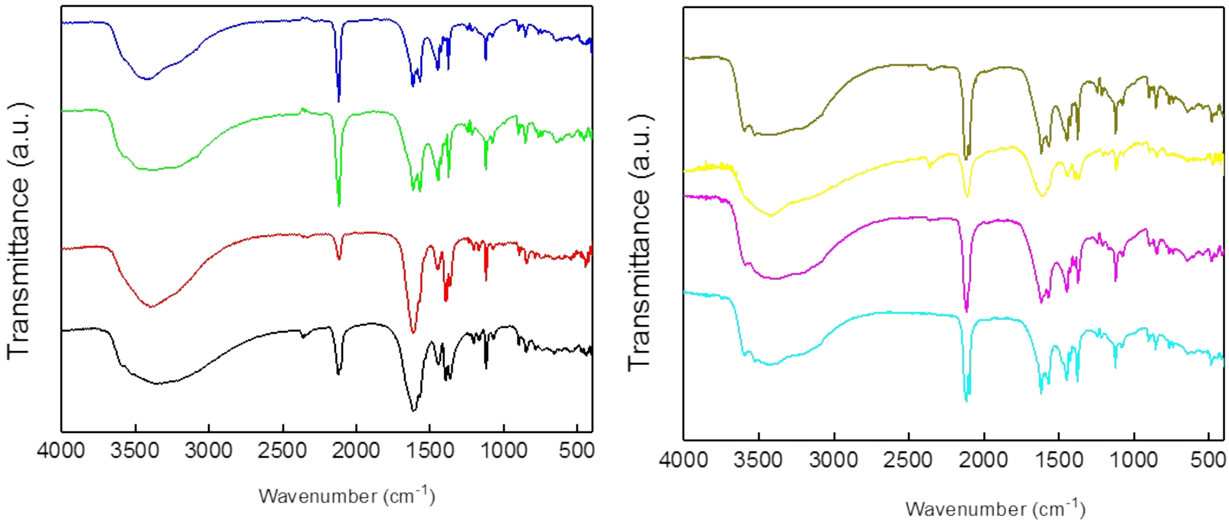

Figure S1. The FTIR of {$KH[Ln_2$(2,3-pzdc)$_2(CH_3OH)(H_2O)_7][MoCN)_8]$}$\cdot 5H_2O$ (left) and {$KH[Ln_2$(2,3-pzdc)$_2(CH_3OH)(H_2O)_7][W(CN)_8]$}$\cdot 5H_2O$ (right). Compounds **1** (black), **2** (red), **3** (green), **4** (blue), **5** (light blue), **6** (pink), **7** (yellow), **8** (tan).

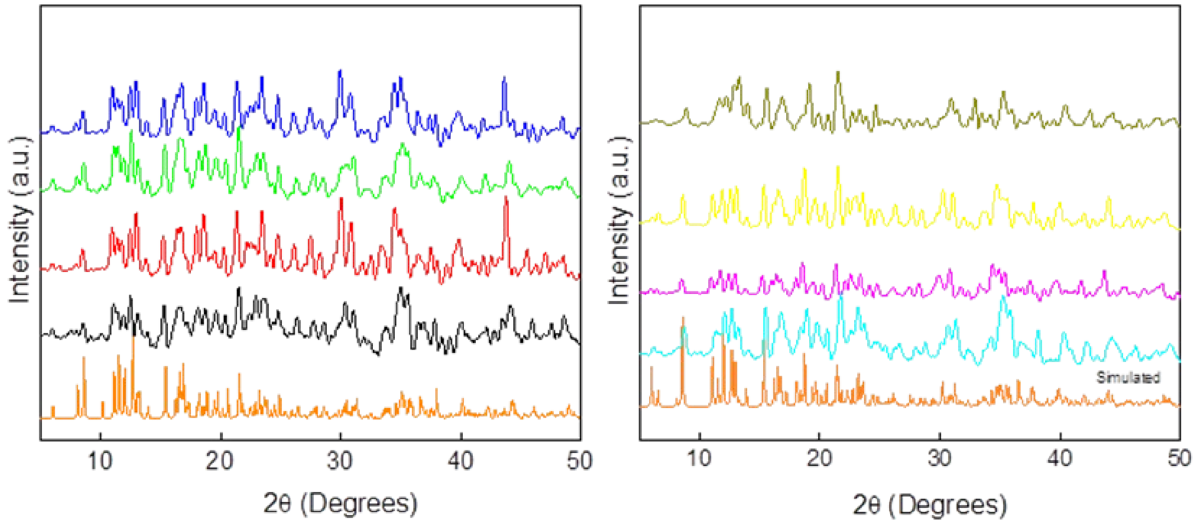

Figure S2. The PXRD of {KH[Ln_2(2,3-pzdc)$_2$(CH_3OH)(H_2O)$_7$][Mo$(CN)_8$]}·5H_2O (left) and {KH[Ln_2(2,3-pzdc)$_2$(CH_3OH)(H_2O)$_7$][W$(CN)_8$]}·5H_2O (right). Compounds **1** (black), **2** (red), **3** (green), **4** (blue), **5** (light blue), **6** (pink), **7** (yellow), **8** (tan) simulated (orange).

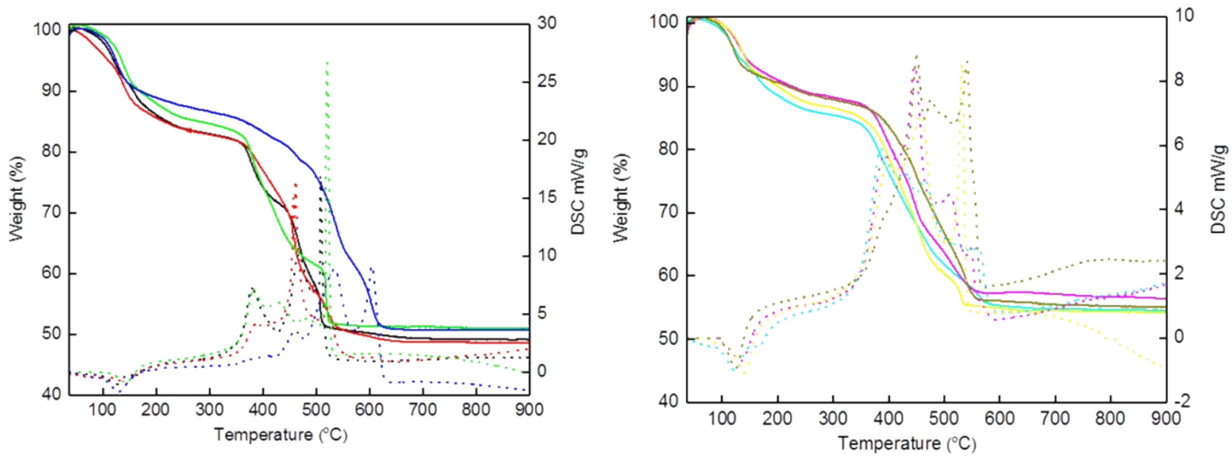

Figure S3. The TGA (line) and the DSC curves (dot) of {KH[Ln_2(2,3-pzdc)$_2$(CH_3OH)(H_2O)$_7$][Mo$(CN)_8$]}·5H_2O (left) and {KH[Ln_2(2,3-pzdc)$_2$(CH_3OH)(H_2O)$_7$][W$(CN)_8$]}·5H_2O (right).Compounds **1** (black), **2** (red), **3** (green), **4** (blue), **5** (light blue), **6** (pink), **7** (yellow), **8** (tan).

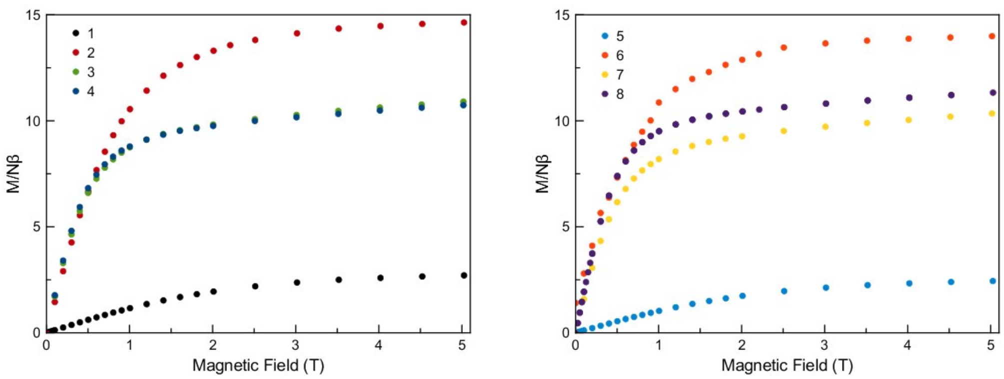

Figure S4. Temperature dependence of the magnetization at 2 K of {KH[Ln_2(2,3-pzdc)$_2$(CH_3OH)(H_2O)$_7$][Mo$(CN)_8$]}·5H_2O, **1−4** (left) and {KH[Ln_2(2,3-pzdc)$_2$(CH_3OH)(H_2O)$_7$][W$(CN)_8$]}·5H_2O, **5−8** (right).

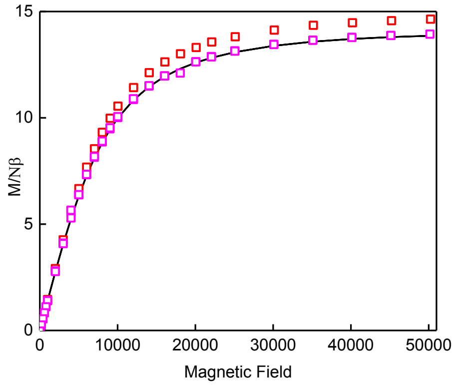

Figure S5. Field dependent of the magnetization of the **2** (red) and **6** (pink) as measured at 2 K. Solid line represents the calculated Brillouin curve for two non-interacting Gd^{3+} ions.

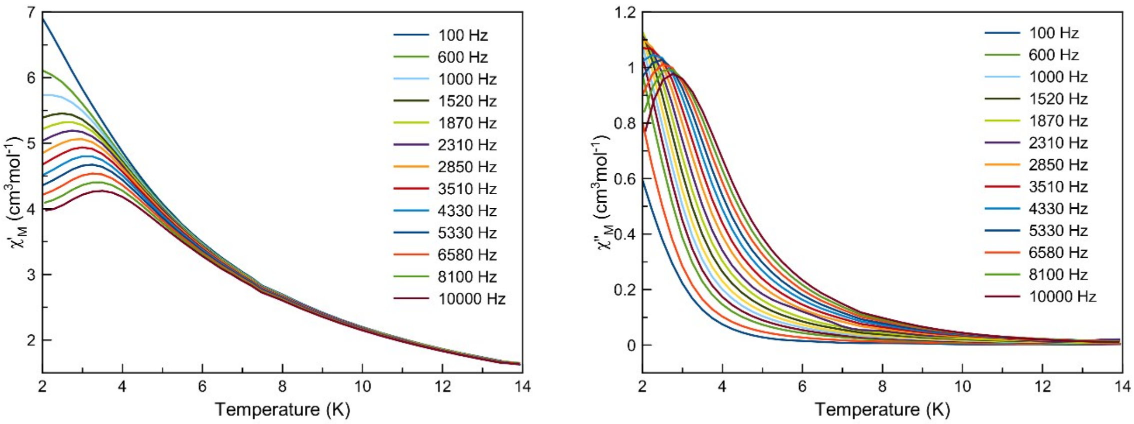

Figure S6. Field dependence of χ'_M and χ''_M of **4** in 1 KOe *dc* applied field.

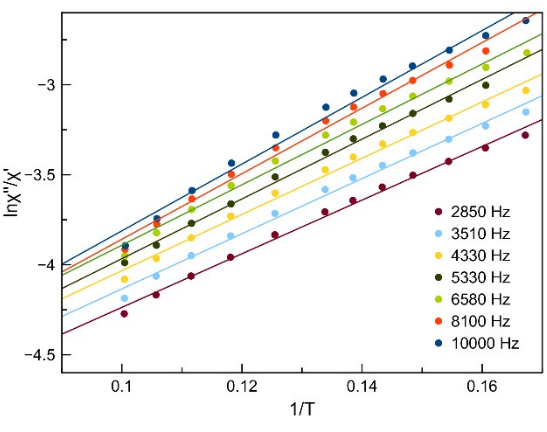

Figure S7. Ln(χ_M''/χ_M') vs 1/T plots for **4** under 1 KOe dc-applied field for frequencies in the range of 2850−10000 Hz. The solid lines are the best linear fits.

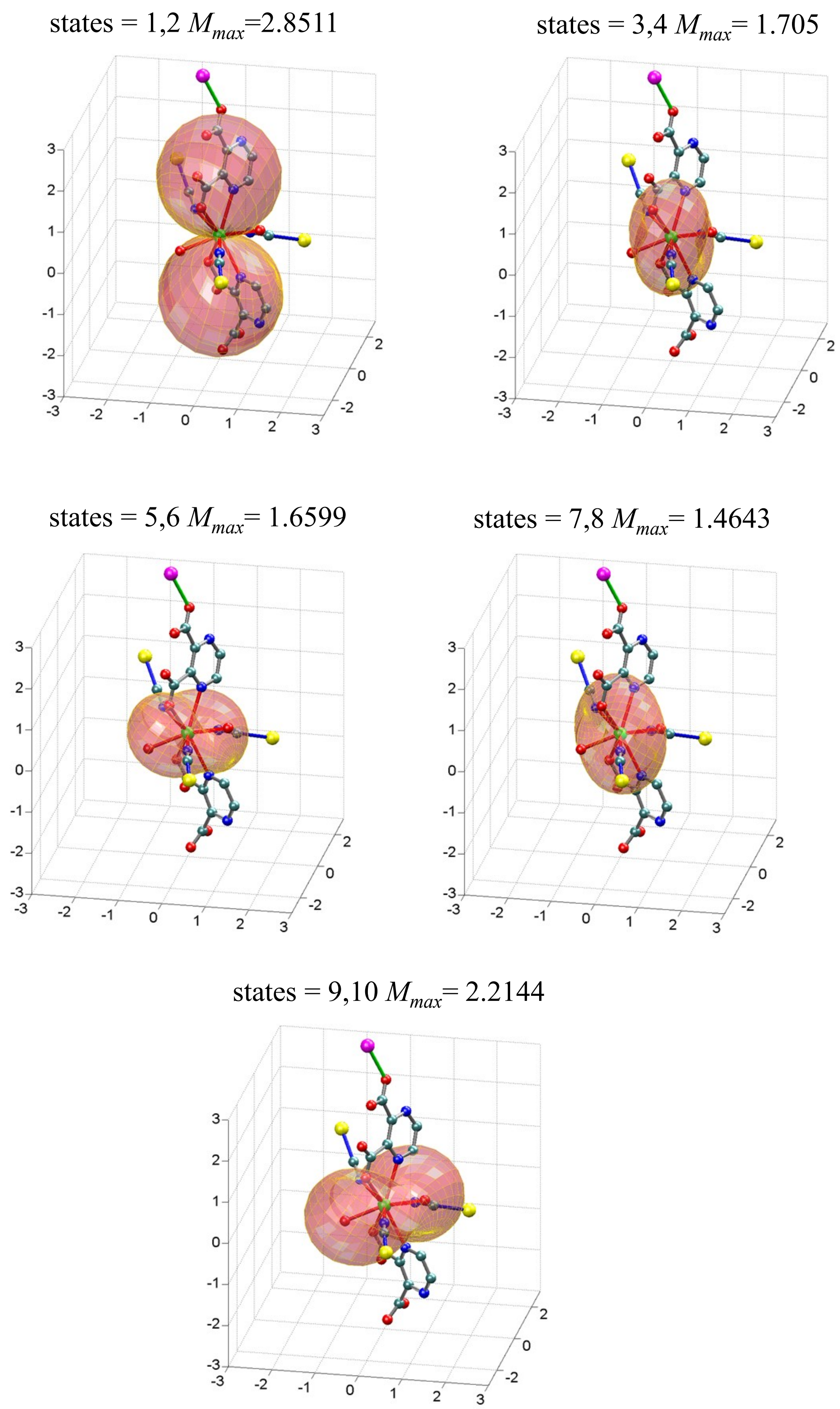

Figure S8. The polar maps of the state-specific magnetization functions for the Nd^{3+} site 1.

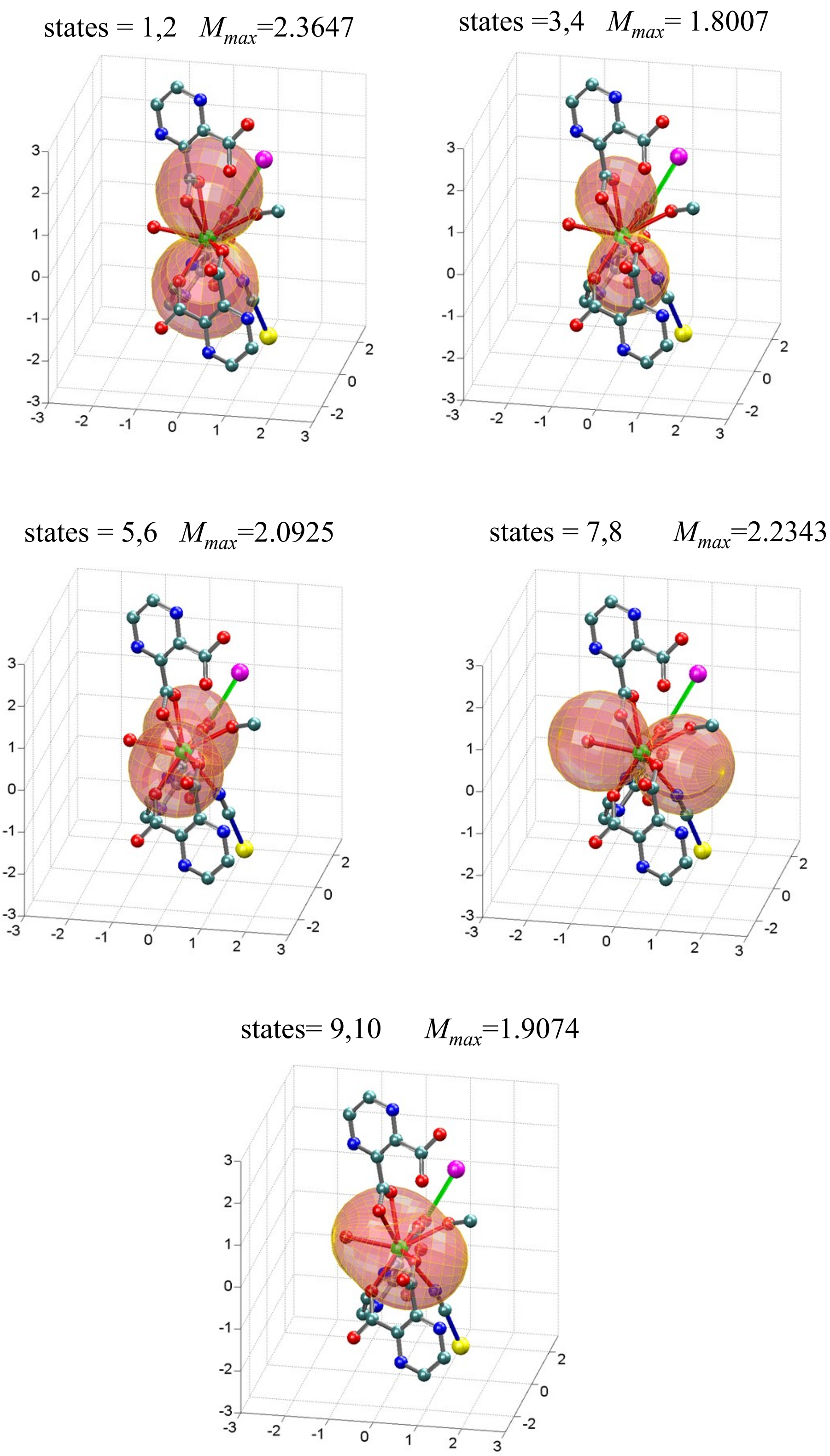

Figure S9. The polar maps of the state-specific magnetization functions for the Nd^{3+} site 2.

states = 1,2 M_{max}= 8.966

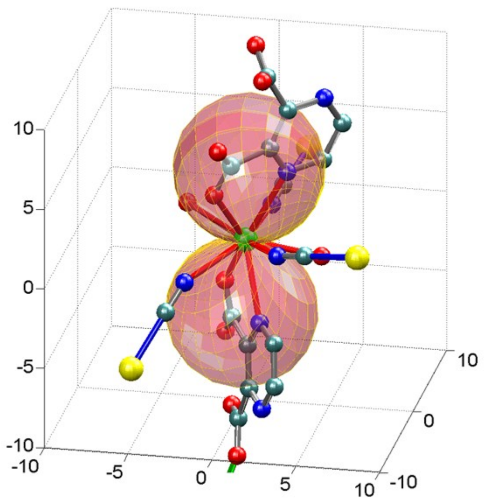

states = 3,4 M_{max}= 6.69

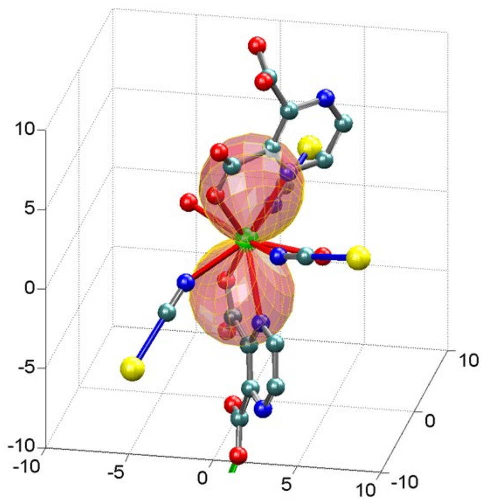

states =5,6 M_{max}= 3.24

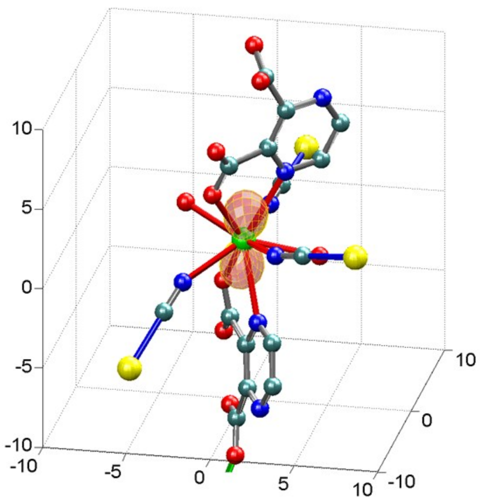

Figure S10. The magnetization polar maps for the states with sizeable effective moment on the Tb^{3+} site 1. Although the states are not organized in rigorously degenerate couples, there are quasi-doublet sequences with closely similar anisotropy features, being represented together (*e.g.* states 1 and 2, displaying only the #1 map). The M_{max} extensions of the lobes for the #5 to #11 states are respectively: 0.569, 0.566, 0.049, 0.277, 0.292, 0.885, 0.889 μB, being barely visible in the chosen representation scale.

states = 1,2 M_{max}= 8.95

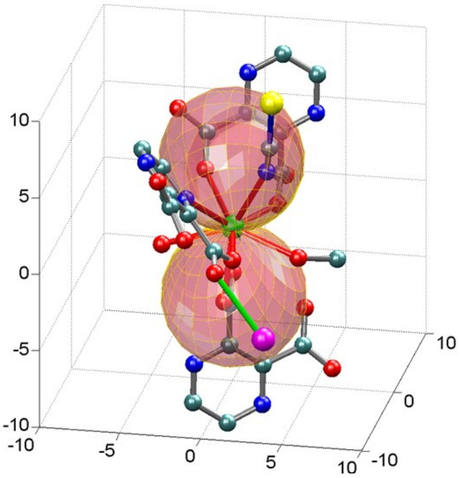

state = 3, 4 M_{max}= 4.94

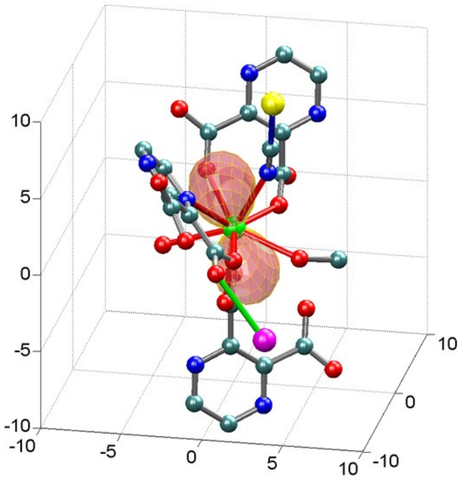

states = 12, 13 M_{max}= 5.33

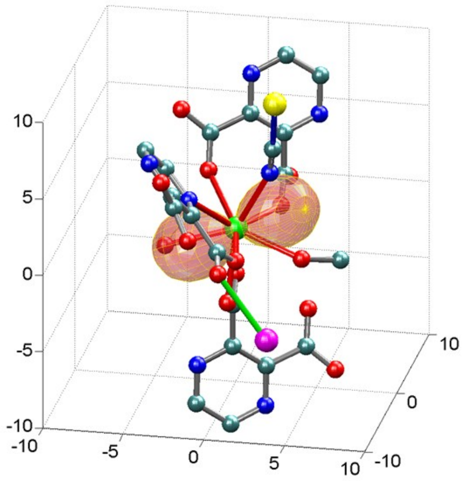

Figure S11. The magnetization polar maps for the states with sizeable effective moment on the Tb^{3+} site 2. The states #7 to #13 states have small lobes, with the following M_{max} extensions: 0.145, 0.145, 0.017, 0.065, 0.039, 0.304, 0.326 μB.

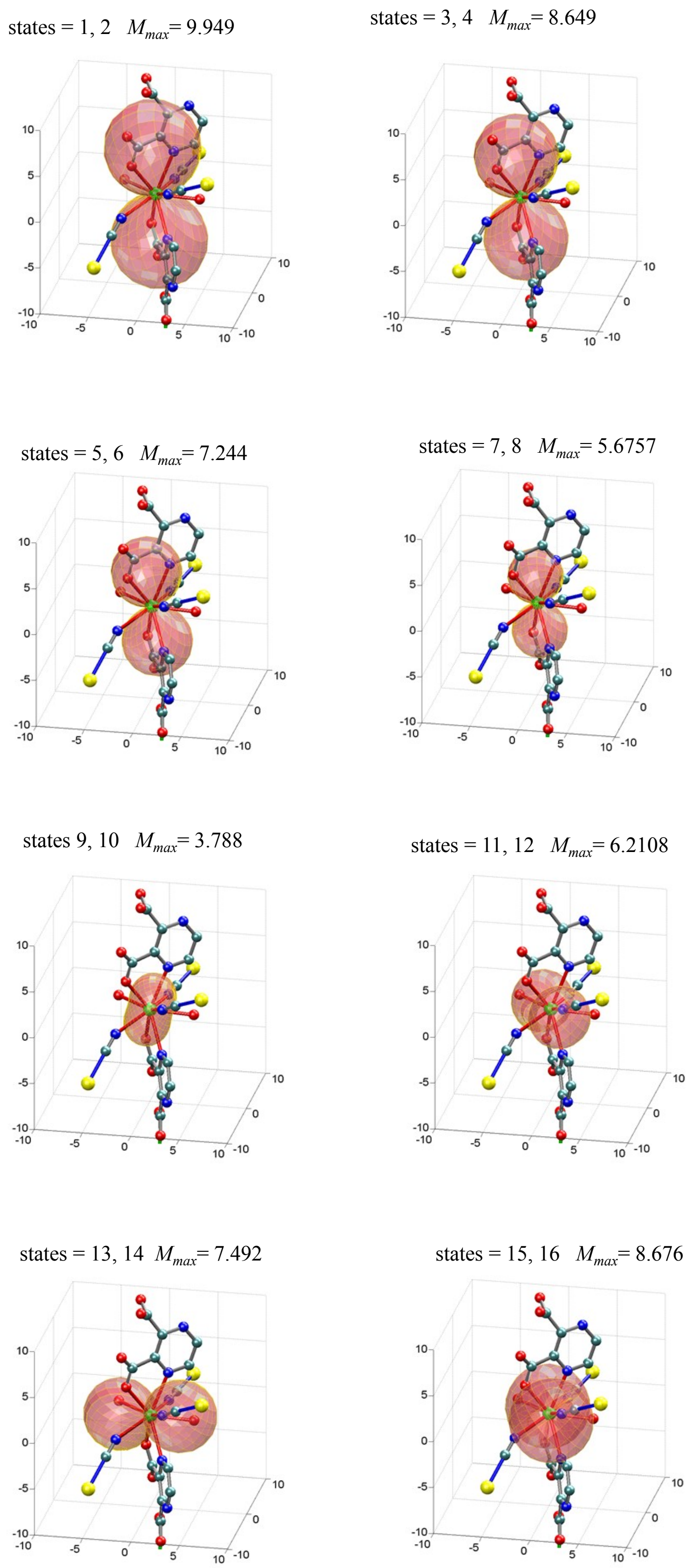

Figure S12. The magnetization polar maps for the states of the Dy^{3+} site 1.

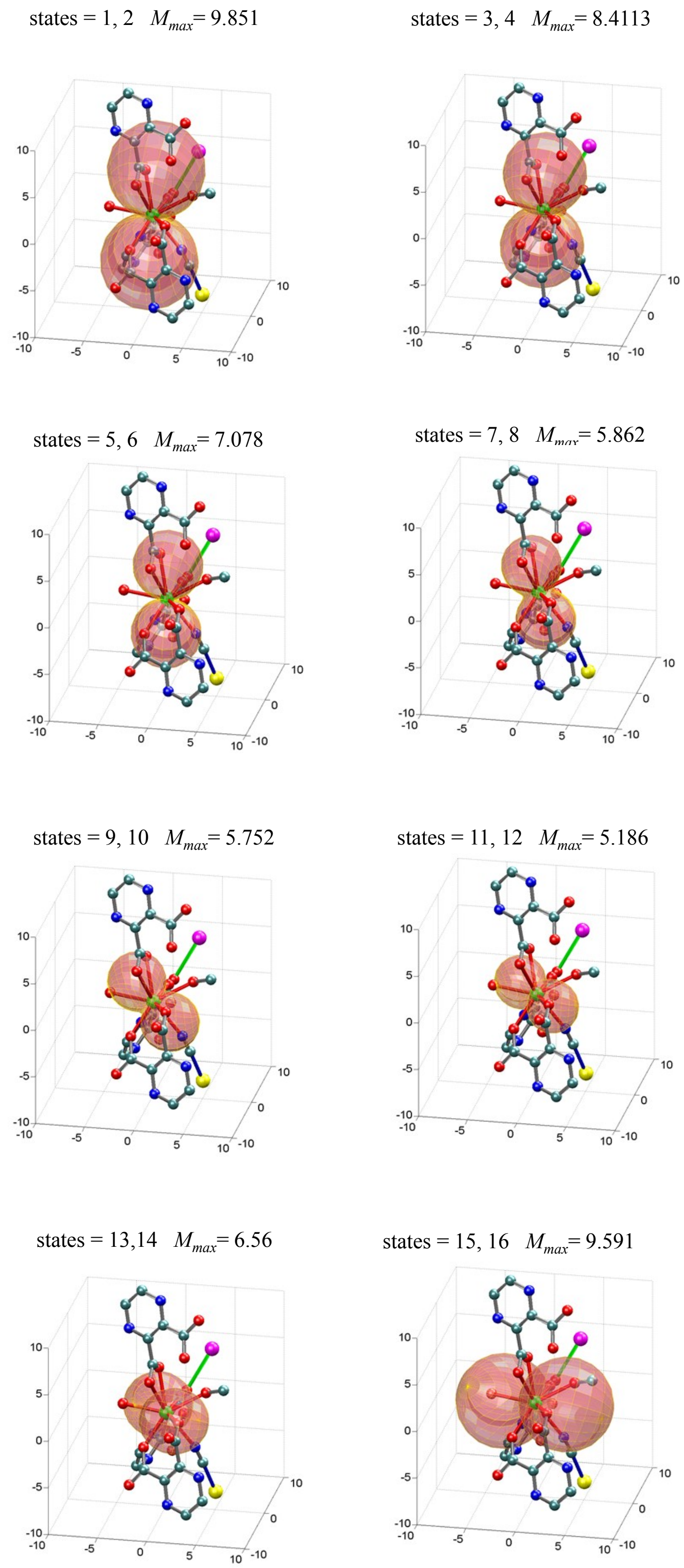

Figure S13. The magnetization polar maps for the states of the Dy^{3+} site 2.

The Ligand Field (LF) analysis is done fitting one-electron part of the *ab initio* computed spectral terms to the following phenomenological Hamiltonian:

$$\hat{H}_{LF}=\sum_{k=2,4,6}\sum_{q>0}^{k}\sqrt{\frac{4\pi}{2k+1}}\left[B_q^k\left(Y_{k,q}+(-1)^q Y_{k,-q}\right)+iB_{-q}^k\left(Y_{k,-q}-(-1)^q Y_{k,q}\right)\right]+\sum_{k=2,4,6}\sqrt{\frac{4\pi}{2k+1}}B_0^k Y_{k,0}$$

The B_q^k numeric parameters resulted for the two sites are given in Tables S1 and S2..

Table S1. The Ligand Field B_q^k parameters (in cm^{-1}) resulted from the Ligand Field analysis of site 1.

				$B_{2,-2}$	$B_{2,-1}$	$B_{2,0}$	$B_{2,+1}$	$B_{2,+2}$				
				-283.8	-83.4	-337.1	-178.3	-87.9				
		$B_{4,-4}$	$B_{4,-3}$	$B_{4,-2}$	$B_{4,-1}$	$B_{4,0}$	$B_{4,+1}$	$B_{4,+2}$	$B_{4,+3}$	$B_{4,+4}$		
		-107.1	-214.2	471.1	121.2	501.8	11.7	-144.3	-277.6	94.0		
$B_{6,-6}$	$B_{6,-5}$	$B_{6,-4}$	$B_{6,-3}$	$B_{6,-2}$	$B_{6,-1}$	$B_{6,0}$	$B_{6,+1}$	$B_{6,+2}$	$B_{6,+3}$	$B_{6,+4}$	$B_{6,+5}$	$B_{6,+6}$
496.4	-175.8	-430.3	-193.9	-15.4	205.4	478.6	-142.8	-152.6	267.8	-31.5	233.3	-362.6

Table S2. The Ligand Field B_q^k parameters (in cm^{-1}) resulted from the Ligand Field analysis of site 2.

				$B_{2,-2}$	$B_{2,-1}$	$B_{2,0}$	$B_{2,+1}$	$B_{2,+2}$				
				188.6	-478.8	-29.8	112.7	-364.9				
		$B_{4,-4}$	$B_{4,-3}$	$B_{4,-2}$	$B_{4,-1}$	$B_{4,0}$	$B_{4,+1}$	$B_{4,+2}$	$B_{4,+3}$	$B_{4,+4}$		
		141.9	386.6	-150.2	53.8	-339.1	-45.7	-134.6	-253.4	110.6		
$B_{6,-6}$	$B_{6,-5}$	$B_{6,-4}$	$B_{6,-3}$	$B_{6,-2}$	$B_{6,-1}$	$B_{6,0}$	$B_{6,+1}$	$B_{6,+2}$	$B_{6,+3}$	$B_{6,+4}$	$B_{6,+5}$	$B_{6,+6}$
630.7	284.5	-73.2	-181.5	-173.3	-419.7	-174.7	-342.8	-282.2	16.6	135.2	305.7	-88.9

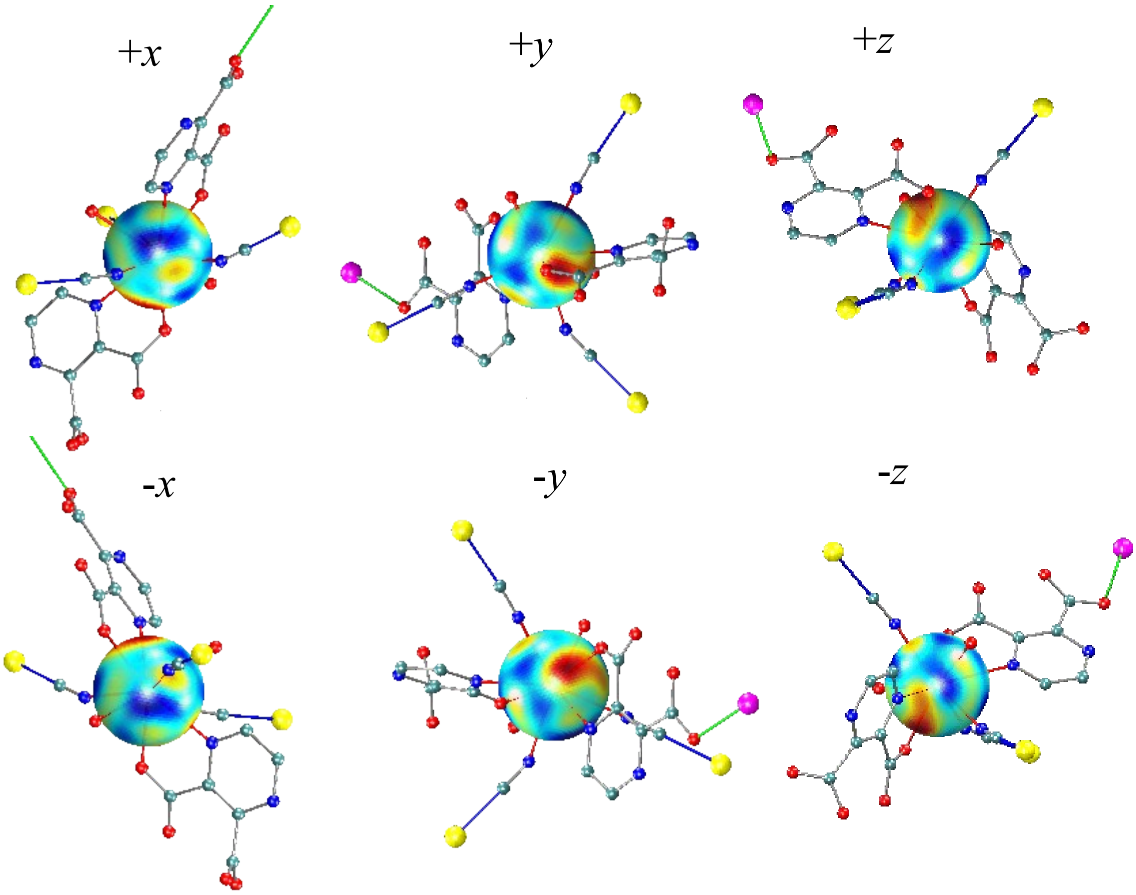

Figure S14. Colormap of the Ligand Field potential for site 1. Different views (along the opposite directions of Cartesian axes). Note the inversion relationships between the elements of upper and lower rows.

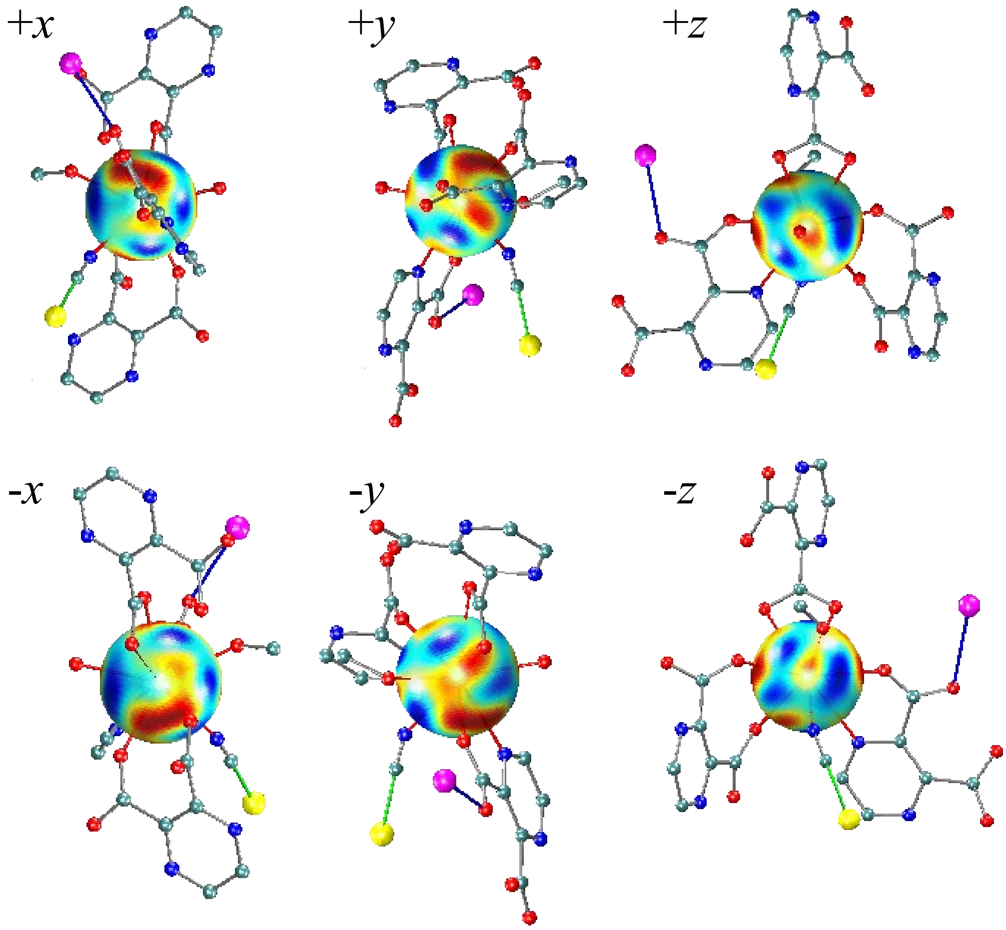

Figure S15. Colormap of the Ligand Field potential for site 2. Different views (along the opposite directions of Cartesian axes). Note the inversion relationships between the elements of upper and lower rows.

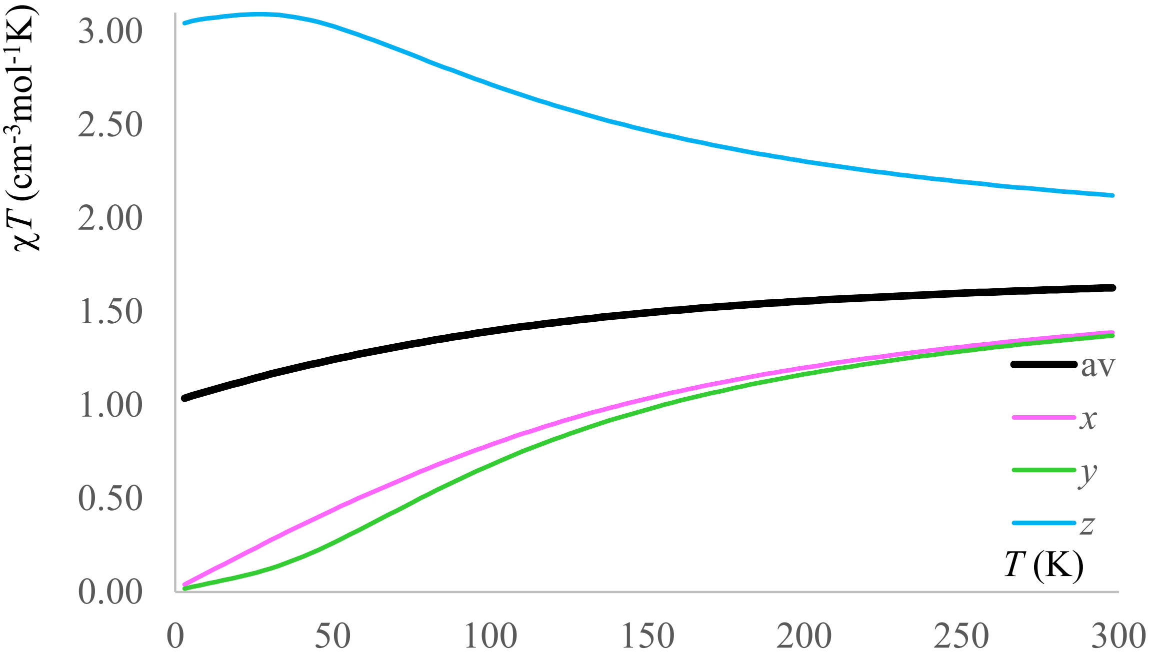

Figure S16. Simulated magnetic susceptibility, shown as T vs. $\chi_M T$ curves for the Nd^{3+} site 1: averaged dependence and anisotropic behavior on Cartesian axes, selecting as ***z*** the easy axis of the ground state level.

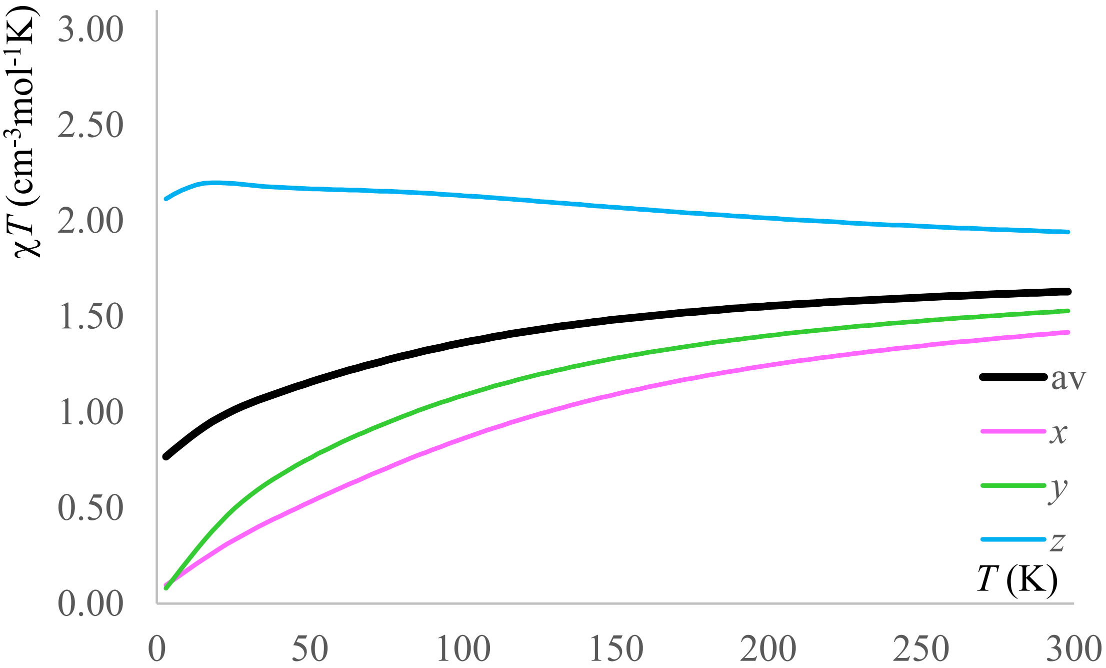

Figure S17. Simulated magnetic susceptibility, shown as T vs. $\chi_M T$ curves for the Nd^{3+} site 2: averaged dependence and anisotropic behavior on Cartesian axes, selecting as ***z*** the easy axis of the ground state level.

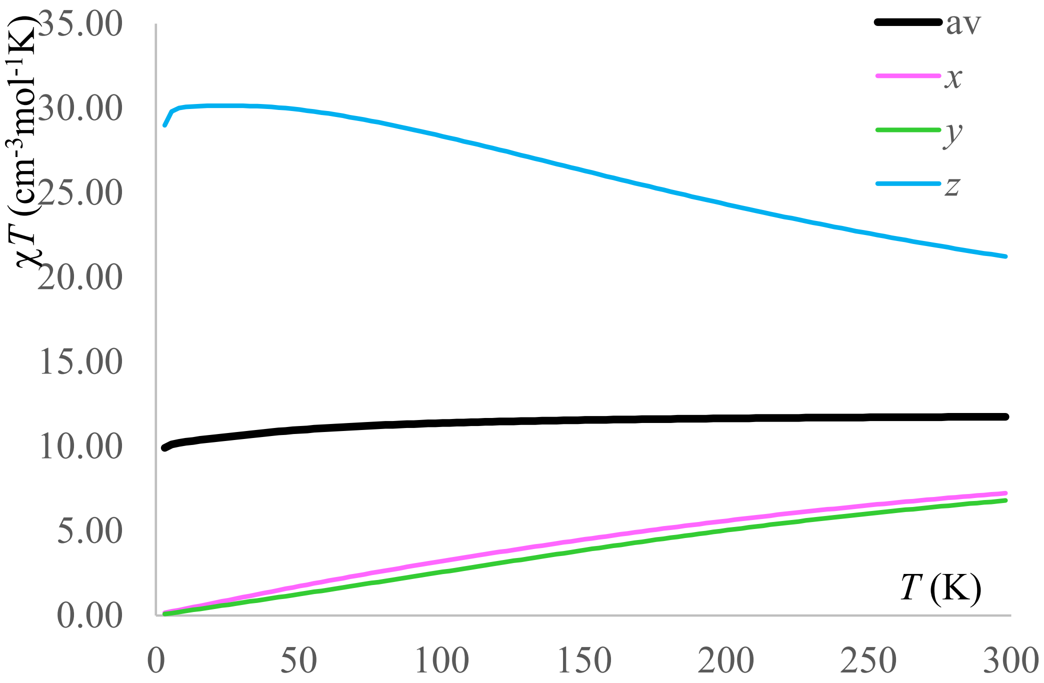

Figure S18. Simulated magnetic susceptibility, shown as *T* vs. $\chi_M T$ curves for the Tb^{3+} site 1: averaged dependence and anisotropic behavior on Cartesian axes, selecting as *z* the easy axis of the ground state level.

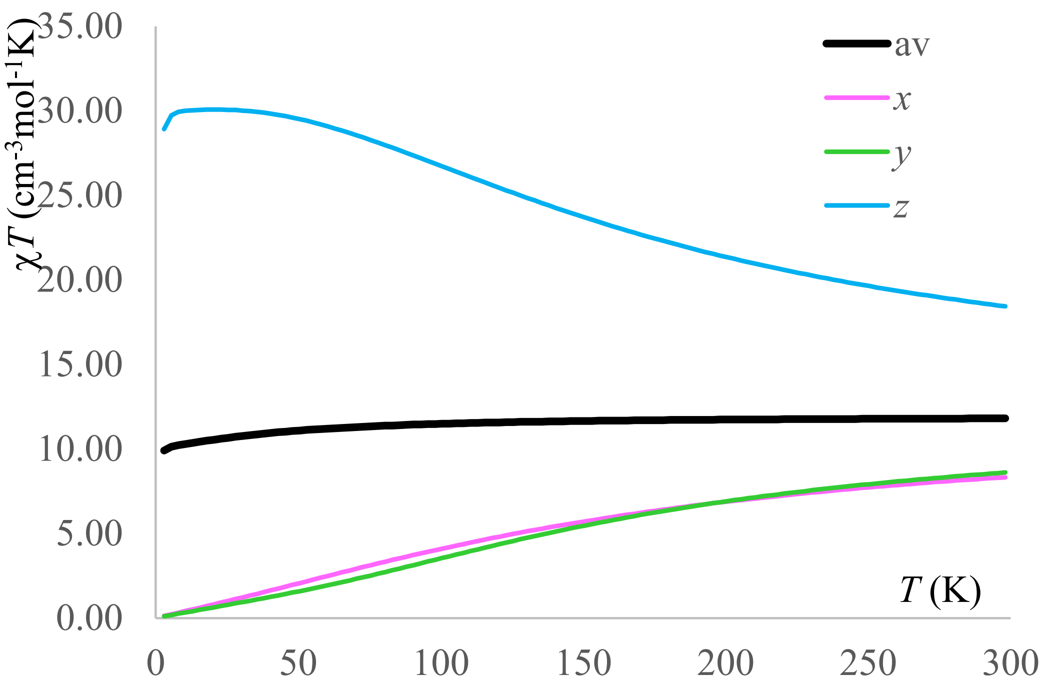

Figure S19. Simulated magnetic susceptibility, shown as *T* vs. $\chi_M T$ curves for the Tb^{3+} site 2: averaged dependence and anisotropic behavior on Cartesian axes, selecting as *z* the easy axis of the ground state level.

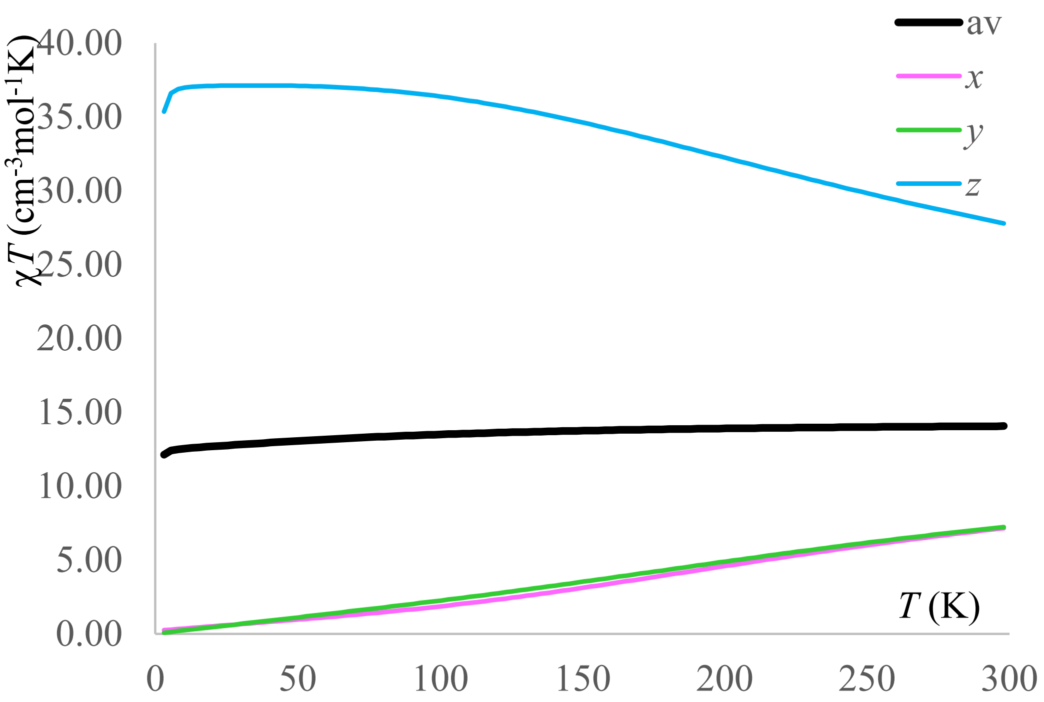

Figure S20. Simulated magnetic susceptibility, shown as *T* vs. $\chi_M T$ curves for the Dy^{3+} site 1: averaged dependence and anisotropic behavior on Cartesian axes, selecting as *z* the easy axis of the ground state level.

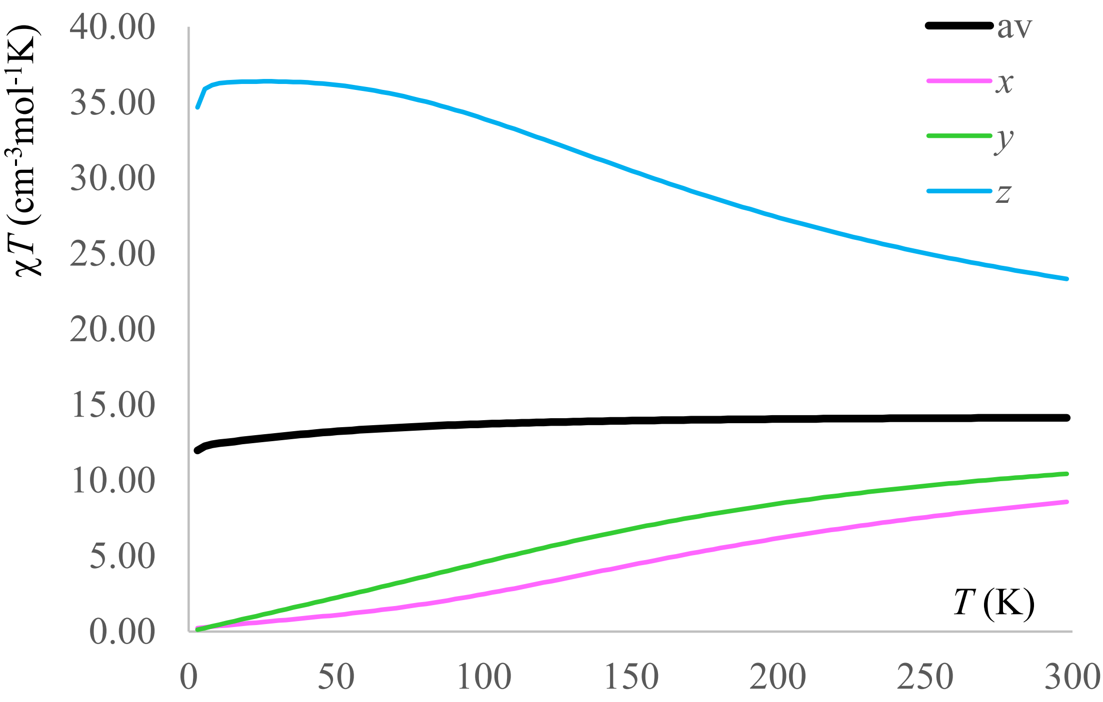

Figure S21. Simulated magnetic susceptibility, shown as *T* vs. $\chi_M T$ curves for the Dy^{3+} site 2: averaged dependence and anisotropic behavior on Cartesian axes, selecting as *z* the easy axis of the ground state level.